NANO LETTERS

pubs.acs.org/NanoLett Letter

2D $In_2Ge_2Te_6$ Crystals for High-Performance p-Channel Transistors

Tong Zhao, Shiying Guo, Xiufeng Song, Jie Gao, Kaili Wang, Xudong Pei, Yujie Yan, Seungwoo Son, Jiamin Lin, Haonan Nie, Biao Xu, Zhesheng Chen, Luca Perfetti, Weigao Xu, Yi Zhang, Shengli Zhang,* Zonghoon Lee, Peng Wang, Xiang Chen,* and Haibo Zeng*

Cite This: *Nano Lett.* 2025, 25, 6235−6243 Read Online

ACCESS | Metrics & More | Article Recommendations | Supporting Information

ABSTRACT: Two-dimensional (2D) semiconductors are ideal channel materials for high-speed, low-power transistors in the post-Moore era due to their high mobility and excellent gate-control capacity. However, most existing 2D semiconductors tend to exhibit either n-type or ambipolar behavior. The limited availability of intrinsic p-type 2D semiconductors significantly restricts their application in logic circuits and integrated circuits. Herein, we present the experimental discovery of high-quality $In_2Ge_2Te_6$ single crystals, which possess a layered structure and exhibit a p-type nature with a low hole-effective mass of 0.27 m_0. The 2D $In_2Ge_2Te_6$ nanosheets, exfoliated from the bulk crystals, show good stability in air, with thickness-dependent variations in Raman peaks and bandgaps. Furthermore, we have successfully developed high-performance 2D $In_2Ge_2Te_6$ p-channel transistors, achieving a hole mobility and on/off current ratio up to 43 $cm^2\ V^{-1}\ s^{-1}$ and 10^5 at room temperature, respectively. Thus, $In_2Ge_2Te_6$ emerges as a promising p-type 2D semiconductor for next-generation electronics.

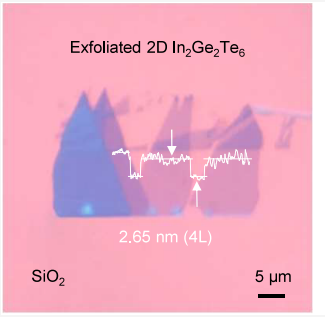

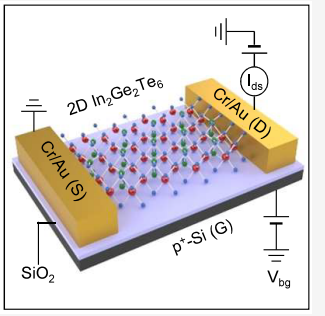

KEYWORDS: *$In_2Ge_2Te_6$, p-type, 2D semiconductor, chemical vapor transport, band structure, field-effect transistors*

The surge in computing demand has hit silicon-based integrated circuits with challenges like short-channel effects, severe heating, and high processing costs.[1,2] Two-dimensional (2D) semiconductors have been considered the ideal channel materials to continue Moore's law for the merits of atomical thickness and no dangling bonds.[3,4] However, most 2D semiconductors studied, particularly transition-metal dichalcogenides (TMDCs), are either n-type or ambipolar due to charge impurities and structural defects.[5] These issues impede the use of p-type semiconductors in high-speed, low-power logic circuits and van der Waals (vdW) heterostructure devices.[6−9] Therefore, there is a pressing need to explore and directly synthesize high-performance intrinsic p-type 2D semiconductors.

$In_2Ge_2Te_6$ is a layered material with a ternary composition, and bulk $In_2Ge_2Te_6$ demonstrates p-type semiconductor behavior with a Seebeck coefficient exceeding 300 $\mu V\ K^{-1}$.[10] Calculations predict that 2D $In_2Ge_2Te_6$ is dynamically stable and functions as a semiconductor with a direct bandgap of 1.4 eV, alongside high carrier mobility exceeding $10^3\ cm^2\ V^{-1}\ s^{-1}$.[11] These characteristics suggest that 2D $In_2Ge_2Te_6$ has substantial potential for future applications in electronics and optoelectronics. Here, we demonstrate that high-quality $In_2Ge_2Te_6$ bulk single crystals, produced using a two-step chemical vapor transportation (CVT) method, exhibit a direct bandgap (E_g) of 0.81 eV and a hole effective mass (m^*) of 0.27. We also obtained a series of 2D $In_2Ge_2Te_6$ nanosheets with a minimum thickness of 0.4 nm (monolayer) from the bulk crystals using mechanical exfoliation (ME). Our findings indicate that the Raman peaks and bandgaps of the nanosheets vary with thickness, and the material exhibits good chemical stability when exposed to air for over two months. Furthermore, we fabricated 2D $In_2Ge_2Te_6$ bottom-gate FET devices, with the highest room-temperature hole mobility and on/off current ratio of 43 $cm^2\ V^{-1}\ s^{-1}$ and 10^5, respectively, achieved at a thickness of 13 nm. This p-type behavior arises from the differing binding forces of Ge−Ge for electrons in the *z* and *xy* directions, which leads to the potential formation of holes in the *xy* direction. In conclusion, we established that 2D $In_2Ge_2Te_6$ is a promising candidate for future electronic and optoelectronic devices due to its p-type nature, suitable bandgap, excellent air stability, low effective mass, and high hole mobility.

$In_2Ge_2Te_6$ is a layered material stacked in an ABC sequence through vdW interactions along the *c*-axis (Figure 1a). The indium atoms (red) are at the center of the octahedra formed

Received: February 6, 2025
Revised: April 1, 2025
Accepted: April 1, 2025
Published: April 3, 2025

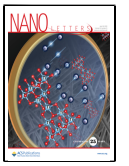

https://doi.org/10.1021/acs.nanolett.5c00580
Nano Lett. 2025, 25, 6235−6243

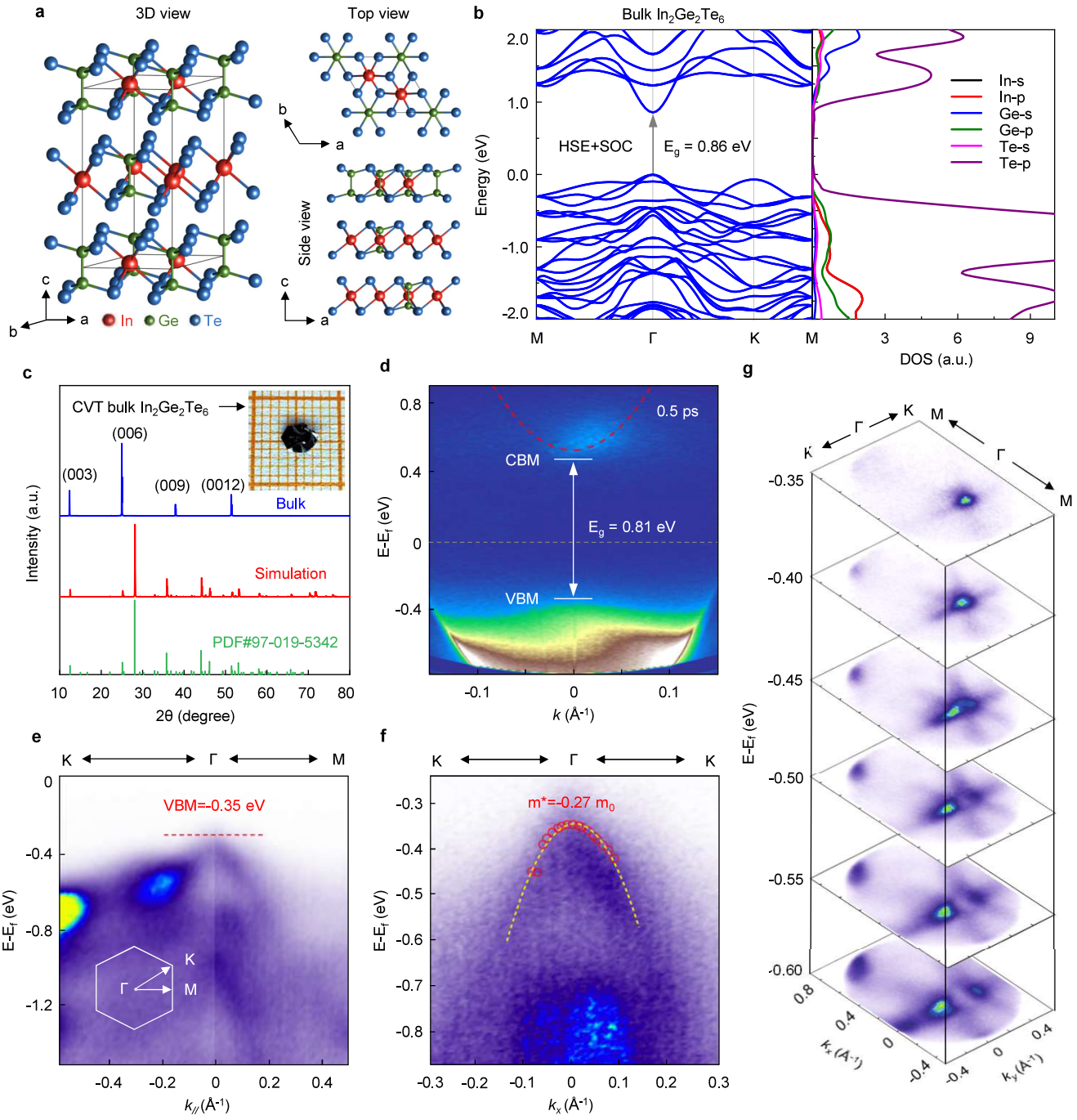

Figure 1. Crystal and electronic structure of bulk $In_2Ge_2Te_6$ single crystals. (a) Layered crystal structure of bulk $In_2Ge_2Te_6$ in 3D view (left), top view (top right), and side view (bottom right). (b) Calculated band structure and DOS of bulk $In_2Ge_2Te_6$ with a direct bandgap of ~0.86 eV. (c) XRD pattern of bulk $In_2Ge_2Te_6$. The embedded image is a photo of a CVT-grown bulk $In_2Ge_2Te_6$ single crystal. (d) Time-resolved ARPES spectra near the Γ point at 0.5 ps pump probe delays for bulk $In_2Ge_2Te_6$ with a direct bandgap of ~0.81 eV. (e) The electronic band structure of bulk $In_2Ge_2Te_6$ measured by spatial-resolved ARPES along the Γ−M−K direction. The inset white hexagon shows the Brillouin zone of bulk $In_2Ge_2Te_6$. The VBM is located at −0.35 eV. (f) Electronic band structure of bulk $In_2Ge_2Te_6$ by a spatial-resolved ARPES test along the Γ−M direction. The yellow dashed lines represent the valence band around the Fermi level, while the red circle represents the hole carrier effective mass, which was determined to be 0.27 through the fitting. (g) The measured point like the Fermi surface map of bulk $In_2Ge_2Te_6$ at a photon energy from −0.35 eV to −0.60 eV. The energy band changes near the Γ point on the Fermi surface demonstrate good hexagonal symmetry.

by the tellurium atoms along the $x-y$ plane. Each germanium atom (green) is bonded to one germanium and three tellurium atoms (blue). The bond lengths for bulk $In_2Ge_2Te_6$ of Ge−Te, Ge−Ge, and In−Te are 2.59 Å, 2.43 Å, and 3.02 Å, respectively. The optimized lattice constant for $In_2Ge_2Te_6$ is $a = b = 7.11$ Å. The detailed structural parameters are listed in Table S1. We analyzed the electronic local function (ELF) of monolayer $In_2Ge_2Te_6$ to investigate its bonding characteristics (Figure S1). It revealed that there is almost no electron localization between In and Te atoms, indicating that the In−Te bonds are ionic in nature. The low ELF value also confirms this. On the other hand, high ELF values between Ge−Ge

https://doi.org/10.1021/acs.nanolett.5c00580
Nano Lett. 2025, 25, 6235−6243

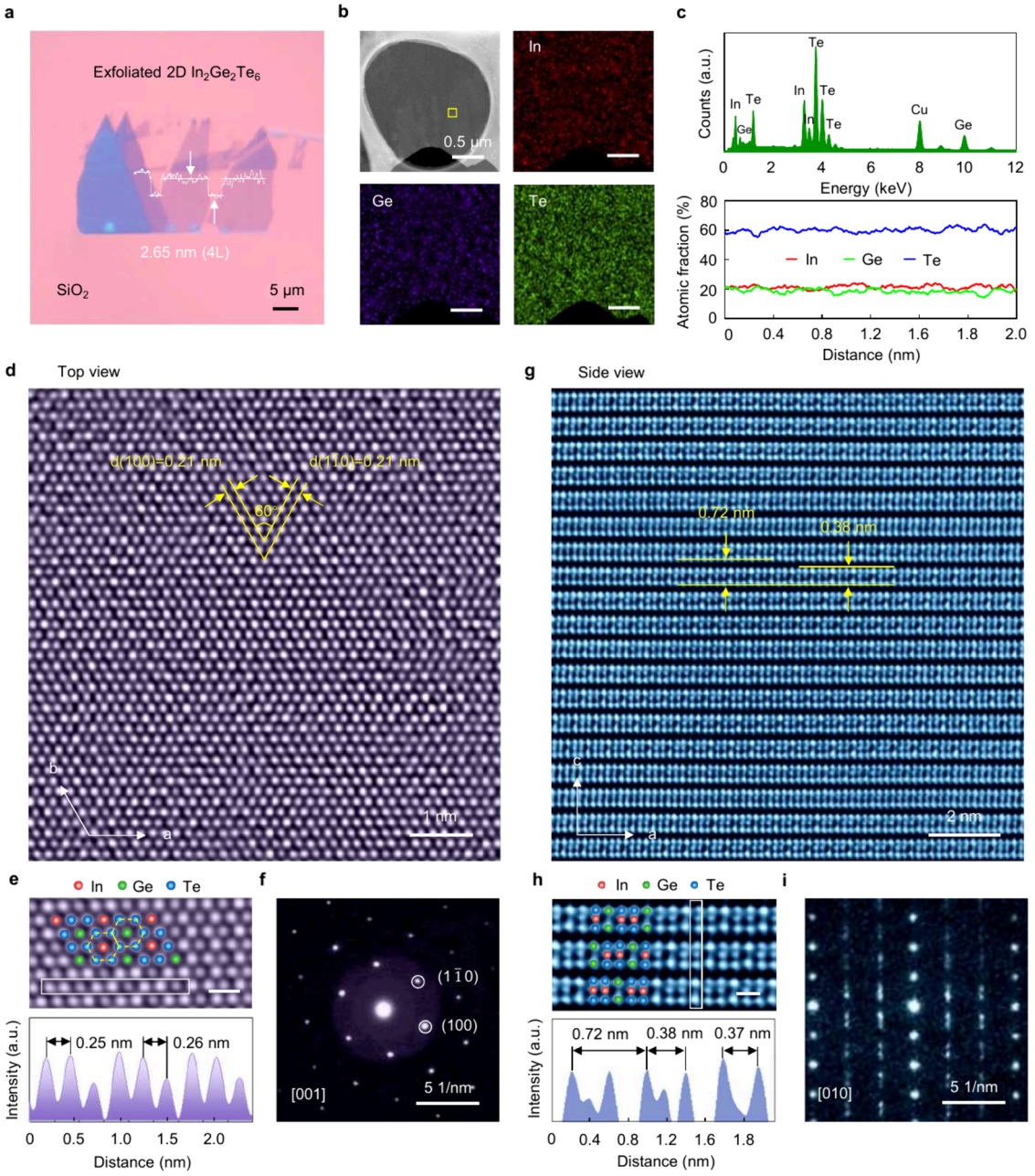

Figure 2. Morphology and atomic structure of 2D $In_2Ge_2Te_3$ nanosheets. (a) OM image and corresponding AFM height profile of 2D layered $In_2Ge_2Te_6$ nanoflakes. (b) Elemental analysis of 2D $In_2Ge_2Te_6$ nanosheets by EDS: In, Ge, and Te elemental mappings, respectively. (c) EDS spectrum and atomic fraction of In, Ge, and Te of $In_2Ge_2Te_6$ in (b). The approximate location of the profile measurement is indicated within the yellow rectangular box in part (b). (d) STEM image of the 2D $In_2Ge_2Te_6$ nanosheets. The atomic resolution image shows that the interplanar spacing is ~0.21 nm. (e) Enlarged STEM image corresponding to (d) and the intensity profile of the purple rectangle region. Scale bar, 0.5 nm. (f) Corresponding SAED pattern of 2D $In_2Ge_2Te_6$ nanosheets. (g) Cross-sectional STEM image of the bulk $In_2Ge_2Te_6$. (h) Enlarged STEM image corresponding to (g) and the intensity profile of the purple rectangle region. Scale bar, 0.5 nm. (i) Corresponding cross-sectional SAED pattern of bulk $In_2Ge_2Te_6$.

suggest some covalent features in the Ge−Ge interaction. This means that the electron distribution centered in the middle of the Ge−Ge bond indicates a covalent bonding connecting the two nearest neighboring $GeTe_3$ tetrahedrons. We also studied the band structure and density of states (DOS) of bulk $In_2Ge_2Te_6$ by the Heyd−Scuseria−Ernzerhof (HSE) function calculation with spin−orbit coupling (SOC) effects. The VBM is located at the Γ point, while the conduction band minimum (CBM) occurs at the Γ point, leading to a direct bandgap of 0.86 eV (Figure 1b). Our analysis of the projected density of states (PDOS) of bulk $In_2Ge_2Te_6$ revealed that the VBM is primarily contributed by the Te-*p* orbital, with some contribution from the Ge-*p* orbital. Two notable resonant peaks in the valence band (VB) regions indicate significant orbital interactions between Te and Ge atoms through *p*−*p* hybridizations. This mitigates the localization of electrons and reduces the scattering in the VB.[12,13] Using first-principles calculations, we also investigated the effective mass and carrier mobility of 2D $In_2Ge_2Te_6$. Our results show that the mono- and bilayer $In_2Ge_2Te_6$ have a low hole effective mass (0.2 and

https://doi.org/10.1021/acs.nanolett.5c00580
Nano Lett. 2025, 25, 6235−6243

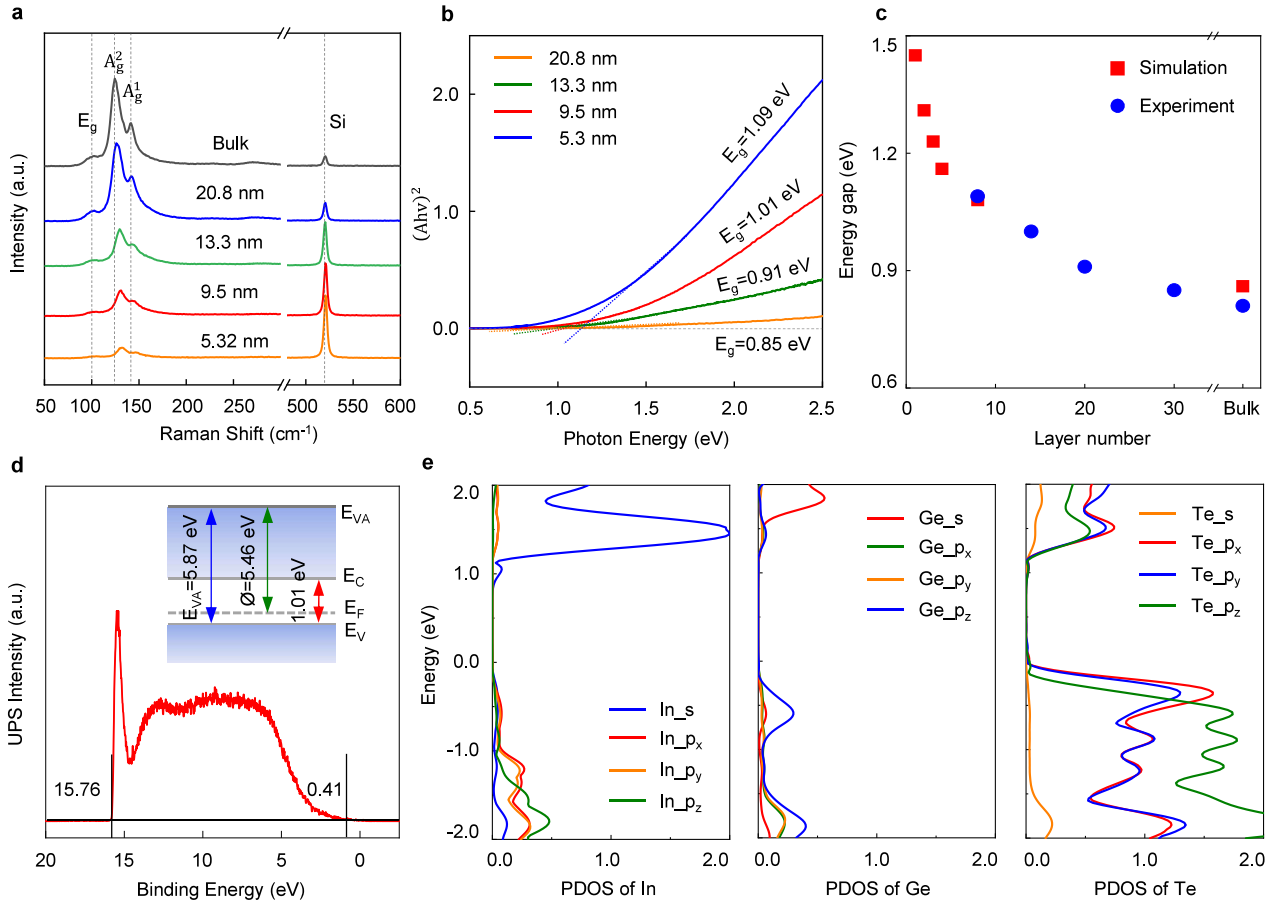

Figure 3. Raman, bandgap spectra and p-type conductive mechanism of 2D $In_2Ge_2Te_6$. (a) Thickness-dependent Raman shift trend of A_g^1 and A_g^2 frequency of $In_2Ge_2Te_6$ nanosheets. (b) The optical bandgap of a series of 2D $In_2Ge_2Te_6$ nanosheets using the UV−vis absorption spectra. (c) The comparison of bandgap and thickness relationships on simulations and experiments. (d) UPS spectra of a 9.5 nm-thick $In_2Ge_2Te_6$ nanosheet, inset: band diagram model obtained from absorption and UPS measurements, where the optical bandgap is 1.01 eV. (e) PDOS of In, Ge, and Te of monolayer $In_2Ge_2Te_6$.

0.16) and high hole mobility (379 and 2271 $cm^2\ V^{-1}\ s^{-1}$), indicating that 2D $In_2Ge_2Te_6$ is a very potential and competitive p-type 2D semiconductor (Table S2).[14]

Conventional CVT methods for synthesizing $In_2Ge_2Te_6$ single crystals often result in the formation of GeTe and In_2Te_3 as undesired byproducts.[11] To overcome this issue, we synthesized high-quality hexagonal $In_2Ge_2Te_6$ by combining the CVT method with presintering. The details of the synthesis can be found in the Supporting Information. First, we examined the X-ray diffraction (XRD) pattern of bulk $In_2Ge_2Te_6$ (Figure 1c). All diffraction peaks of bulk $In_2Ge_2Te_6$ are indexed well to the (003n) direction, confirming that the sample had grown preferentially along the *c* direction. The inset in Figure 1c shows the single-crystalline bulk $In_2Ge_2Te_6$ crystal with a hexagonal shape, measuring 5 mm in size. We used time-resolved ARPES to observe the electronic band structure of bulk $In_2Ge_2Te_6$ and identify its ultrafast electronic dynamics and unoccupied electronic states. The results show a direct bandgap with 0.81 eV (Figure 1d). Photoluminescence (PL) measurements reveal that bulk $In_2Ge_2Te_6$ exhibits an optical bandgap of 0.84 eV (Figure S6), which in close agreement with the bandgap of 0.81 eV determined by tr-ARPES. We further explored the electronic band structure of bulk $In_2Ge_2Te_6$ using spatial-resolved ARPES tests. The overall highly symmetric bands along Γ−K and Γ−M confirm the position of VBM located at the Γ point at −0.35 eV (Figure 1e), and the inset is the Brillouin zone of the $In_2Ge_2Te_6$ lattice.[15] Due to the direct band being 0.81 eV and the VBM at −0.35 eV, the VBM is closer to the Fermi level, indicating that bulk $In_2Ge_2Te_6$ is a p-type semiconductor with a direct bandgap. More importantly, we observed a very low in-plane hole effective mass of $m^* = 0.27$ by fitting the VB mapped out by ARPES (Figure 1f; for more details, see Figure S7). We compared the performance of our material and other published p-type 2D semiconductors, focusing on the effective mass surveying by ARPES (Figure S8 and Table S3). In theory, a lower effective mass correlates with higher mobility in p-type 2D semiconductors, making them excellent candidates for electronic applications. The hole effective mass of 2D $In_2Ge_2Te_6$ is ∼0.27, comparable to conventional p-type 2D semiconductors like WSe_2 and SnS, smaller than TeO_2, GaSe, and GeTe.[16−19] This suggests that 2D $In_2Ge_2Te_6$ has significant potential for further improvement in hole mobility. While BP exhibits better effective mass than $In_2Ge_2Te_6$, the former offers terrible air stability, making it unsuitable for practical applications.[20,21] In addition, the stacking plots of constant energy contours from −0.60 eV to −0.35 eV indicate that the band fluctuations show evident 6-fold symmetry around the VBM at the Γ point, matching well with the theoretical simulation results of $In_2Ge_2Te_6$ being a hexagonal lattice structure (Figure 1g).

https://doi.org/10.1021/acs.nanolett.5c00580
Nano Lett. 2025, 25, 6235−6243

We exfoliated 2D $In_2Ge_2Te_6$ nanosheets successfully, which is beneficial in investigating the structural and physical properties at the 2D atomic scale. The optical microscopy (OM) image shows exfoliated 2D $In_2Ge_2Te_6$ nanosheets with a thickness of 2.65 nm, corresponding to 4 layers (4L) (Figure 2a). It is further accessible to obtain 2D $In_2Ge_2Te_6$ with thinner thicknesses (Figure S10). An energy dispersive spectroscopy (EDS) test verifies that the 2D $In_2Ge_2Te_6$ is composed solely of In, Ge, and Te. Meanwhile, the homogeneous color distribution of the elemental mapping indicates the highly uniform distribution of the three elements in the whole nanosheet (Figure 2b). The atomic fractions of In, Ge, and Te obtained from a line sweep of Figure 2b are roughly in the ratio of 1:1:3, as shown in Figure 2c. To better understand the crystal structure and confirm the quality of 2D $In_2Ge_2Te_6$ nanosheets, we used HAADF-STEM to analyze the in-plane and cross-sectional atomic arrangements. Our observations show that the 2D $In_2Ge_2Te_6$ nanosheets have high crystallinity, as we did not detect any significant defects in the in-plane STEM image (Figure 2d). We measured the crystalline interplanar lattice spacing to be 0.21 nm, which corresponds to the $(1\bar{1}0)$ and (100) planes of the hexagonal $In_2Ge_2Te_6$ crystal. Additionally, the angle between the two crystal planes is 60°, consistent with the calculated lattice structure. By analyzing the contrast of different atoms, we were able to determine the atomic arrangement of 2D $In_2Ge_2Te_6$ (Figure 2e). This arrangement shows that an In atom is surrounded by six Te atoms, and a Ge atom is also surrounded by six Te atoms, which is consistent with the top view atomic structure simulated in Figure 1a. Moreover, the selected area electron diffraction (SAED) patterns with a set of single-crystalline scattered bright spots illustrate the hexagonal structure of 2D $In_2Ge_2Te_6$ (Figure 2f). The patterns show the crystalline phase of $(1\bar{1}0)$ and (100), and the intersection angles of each other match well with the information displayed in the HAADF-STEM image. All the above findings demonstrate that the exfoliated 2D $In_2Ge_2Te_6$ nanoflakes are of excellent crystal quality. We analyzed the cross-sectional image of $In_2Ge_2Te_6$ using the focused ion beam (FIB) method to better understand the crystal structure of layered $In_2Ge_2Te_6$. We aimed to determine the layered structure's thickness, spacing, and stacking mode. The cross-sectional HAADF-STEM image confirms the layered structure and vdW gap (Figure 2g). It also shows the arrangement of atoms along the *c*-axis, with three atoms matching Te−In−Te atoms and two atoms corresponding to Ge−Ge atoms, as well as Te−In−Te, Te−In−Te, and Ge−Ge atoms alternately arrayed in each layer. The atomic arrangement between layers confirms the simulated structure of layered $In_2Ge_2Te_6$ with the ABC stacking mode. We measured the lattice spacing of 0.72 nm along the *c*-axis and the atomic height of each layer as 0.38 nm through the intensity line profiles, consistent with the simulation results of 0.711 and 0.388 nm. We also deduced that the vdW gap is 0.34 nm. The above results are presented in Figure 2h. The SAED patterns show scattered bright spots along the *c*-axis, illustrating the layer structure of $In_2Ge_2Te_6$ crystals (Figure 2i).[22]

To explore layer-dependent characteristics corresponding to both lattices, we perform a series of Raman characterizations of different thickness $In_2Ge_2Te_6$ with a green laser (λ = 532 nm) in the air. The typical Raman spectrum of the $In_2Ge_2Te_6$ single-crystal flakes ranging from 50 to 600 cm^{-1} is presented in Figure 3a. We observed three peaks of 20.8 nm thickness $In_2Ge_2Te_6$ flakes located at 101 cm^{-1}, 125 cm^{-1}, and 142 cm^{-1}, which can be assigned to E_g, A_g^2, and A_g^1 modes, respectively. E_g and A_g present the in-plane and out-of-plane vibration. Moreover, we found that the A_g^2 and A_g^1 modes exhibit redshifts with increasing sample thickness, while the E_g mode has a relatively weak dependence on the thickness. According to the classical model of coupled harmonic oscillators, the E_g, A_g^2, and A_g^1 modes are, in principle, blue-shifted; however, the A_g^1 and A_g^2 modes show a visible redshift. In ultrathin 2D materials, the quantum confinement effect is pronounced, leading to the localization of atomic wave functions. As the thickness increases, the wave functions gradually delocalize, weakening the quantum confinement effect. This results in a decrease in the vibrational mode frequencies, thereby causing a redshift.[23,24] Meanwhile, the thickness-insensitive behavior of the E_g mode may be due to the long-range interlayer Coulomb interactions.[25,26] The stability of p-type semiconductor materials in air significantly affects their application prospects. Therefore, we investigated the air stability of 2D $In_2Ge_2Te_6$ by leveraging Raman spectroscopy. The results demonstrated 2D $In_2Ge_2Te_6$ exhibits excellent ambient air stability. We studied the influence of thickness on the band structure of 2D $In_2Ge_2Te_6$, using micro infrared absorption spectroscopy and first-principles calculations of density functional theory (DFT). Experimentally, we measured the optical absorption properties of 2D $In_2Ge_2Te_6$ nanosheets with different thicknesses. Our findings show that the absorption capacity of thicker nanosheets is significantly higher than that of thinner nanosheets, and the absorption band edge has a redshift as the thickness increases. This indicates that the bandgap width is reduced. A formula can calculate the energy gap value.

$$(Ahv)^n = B(hv - E_g) \tag{1}$$

where B is the constant coefficient and hv is the energy of the incident photons. n = 2 when the material is a direct bandgap semiconductor, and n = 0.5 when the material is an indirect bandgap semiconductor. By plotting the $(Ahv)^2$ curve proportional to the (hv) curve, we calculated the effective optical bandgap of the 2D $In_2Ge_2Te_6$ of different thicknesses (Figure 3b). We observed that the optical absorption bandgaps of synthesized crystals with a thickness of 5.1, 9.5, 13.3, and 17.0 nm are approximately 1.09, 1.01, 0.91, and 0.85 eV, respectively. Theoretically, the HSE patterns with SOC of the bandgap for monolayer, bilayer, trilayer, and four-layer $In_2Ge_2Te_6$ were calculated. Their corresponding bandgaps are ∼1.45 eV, ∼1.31 eV, ∼1.23 eV, and ∼1.16 eV, respectively (Figure S13). To clearly compare the experimental results and DFT theoretical calculations, we separately calculated the bandgap values corresponding to different thicknesses in theory and experiment (the points in Figure 3c). It can be seen that both theoretically and experimentally, the bandgap increases with the decrease in thickness, and the variation pattern is almost the same. This trend is primarily attributed to the amplification of quantum confinement effects in 2D structural systems. Electrons in 2D materials are confined vertically, and reducing the thickness will boost electron interaction, strengthen the confinement effect, and consequently increase the energy gap.[27]

We used ultraviolet photoelectron spectroscopy (UPS) and absorption spectra to investigate the energy band diagram of $In_2Ge_2Te_6$ nanoflakes (9.5 nm). The formula is as follows:

https://doi.org/10.1021/acs.nanolett.5c00580
Nano Lett. 2025, 25, 6235−6243

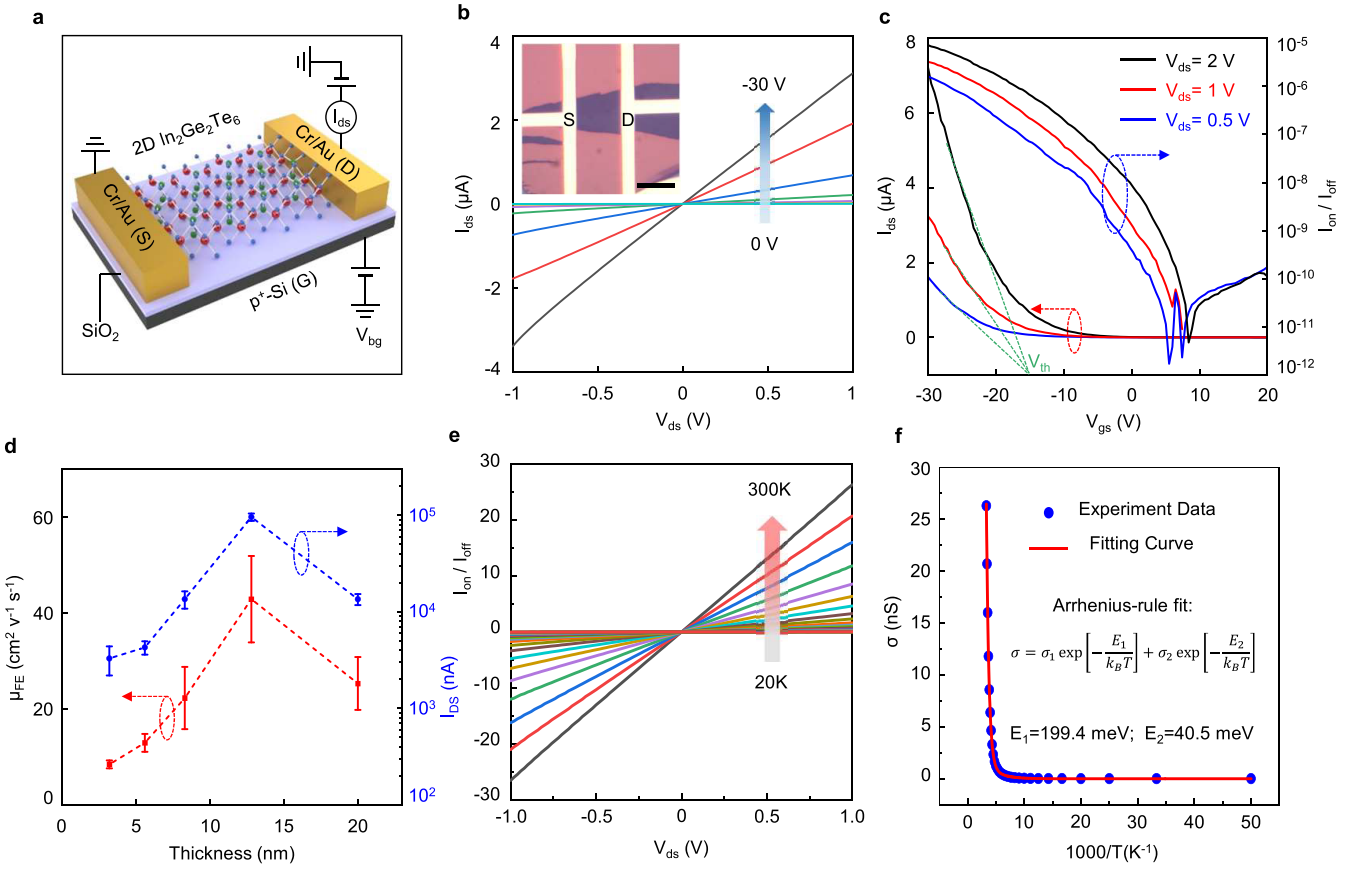

Figure 4. Field-effect transistor performance of p-type 2D $In_2Ge_2Te_6$. (a) Schematic of the back-gate 2D $In_2Ge_2Te_6$ FET device. The gate is p^+-Si, and the source and drain contacts are Cr/Au (3/60 nm). (b) Output curves of the 2D $In_2Ge_2Te_6$ FET device under different back-gate voltage (range from −30 to 0 V). Inset: OM image of the 2D $In_2Ge_2Te_6$ FET device; scale bar, 5 μm. The thickness of the $In_2Ge_2Te_6$ nanoflake is ∼13 nm. (c) Transfer I_{ds}−V_{gs} curves of a 13 nm-thick $In_2Ge_2Te_6$ nanoflake FET device under 0.5, 1, and 2 V drain voltage. (d) Field-effect mobilities and on/off ratio as a function of thickness of 2D $In_2Ge_2Te_6$-based FETs, in which results are extracted from six devices with thicknesses from 3 to 22 nm. The error bars represent the statistical variation obtained from multiple measurements on the same device under different drain−source voltages (V_{ds} = 0.5, 1, and 2 V). (e) Temperature-dependent output I_{ds}−V_{ds} curves of the $In_2Ge_2Te_6$ FET device (range from 20 to 300 K). (f) σ−1000/T (20−300 K) plot and the Arrhenius-rule fit curve.

$$W_f = HV - (E_{cutoff} - E_f) \quad (2)$$

where hv is the incident photon energy (21.2 eV) and the E_{cutoff} is the onset level associated with secondary electrons. We found that the W_f of $In_2Ge_2Te_6$ is 5.46 eV. The VB is located at 0.41 eV below the Fermi energy (E_F) by linearly extrapolating the leading edge of the spectrum to the baseline (Figure 3d). Moreover, the absorption spectra (Figure 3b) revealed that the optical bandgap of the 9.5 nm $In_2Ge_2Te_6$ nanoflake is ∼1.01 eV. Therefore, we determined the energy band diagram and displayed it in the inset of Figure 3d. The Fermi level is closer to the VBM than the CBM, indicating the intrinsic p-type semiconductor characteristic of 2D $In_2Ge_2Te_6$. To further investigate the p-type nature of this material, we calculated the electronic band structure of monolayer $In_2Ge_2Te_6$. We found that it has a direct bandgap of 1.45 eV (Figure S13) and examined the PDOS of the state of In, Ge, and Te (Figure 3e) at the HSE06 level. The Te atoms in the VB closer to the Fermi level have p_x, p_y, and p_z orbitals with similar energies. This similarity can also be observed in the p_x, p_y, and p_z orbitals of In atoms. Thus, the In-p and Te-p orbitals are hybridized similarly to nearby atoms in the x, y, and z directions, resulting in approximately equal binding forces for electrons. In contrast, as shown in Figure 3e, the Ge atoms' energy of p_z orbitals is substantially higher than that of p_x and p_y orbitals, implying that the p_z suborbitals in the VB contribute significantly more to the p_z orbitals than p_x and p_y. Upon analyzing the ELF (Figure S1), we found that Ge−Ge exhibits covalent bonding capabilities along the z-axis direction, exerting significant binding forces on electrons and focusing between the two atoms. Ge−Te also shows covalent bonding capabilities along the xy axis. However, due to the significant hybridization between the Ge-p and Te-p orbitals, electrons are predominantly confined around Te atoms, raising the potential of holes near Ge. We speculate that the p-type characteristic of 2D $In_2Ge_2Te_6$ originates from the different binding forces of Ge−Ge for electrons in the z and xy directions, which leads to the potential formation of holes in the xy direction.[28]

We conducted research on the electrical properties of 2D $In_2Ge_2Te_6$ by creating bottom-gate FET devices with Cr/Au (3 nm/60 nm) as the drain and source electrodes (Figure 4a). To investigate the electrical transport properties of a 13 nm-thick $In_2Ge_2Te_6$ FET, we measured I_{ds}−V_{ds} output and I_{ds}−V_{gs} transfer curves. The output characteristic curve showed a good linear relationship, indicating that the metal electrode and channel material formed an ohmic contact (Figure 4b). The transfer curves were from a set of V_{gs} and I_{ds} with the application of V_{ds} from 0.5 V to 2 V (Figure 4c). The on-state current reached 10^{-5} Å, and the off-state current could be

https://doi.org/10.1021/acs.nanolett.5c00580
Nano Lett. 2025, 25, 6235−6243

reduced to 10^{-10} Å. The switching ratio of the 2D $In_2Ge_2Te_6$ FET reached ~10^5, which could realize the current off. We calculated the estimated room-temperature field-effect mobility (μ) as a function of V_{gs} by using the following equation:

$$\mu = \frac{L}{V_{ds} W C_i} \frac{dI_{ds}}{dV_{gs}} \quad (3)$$

where L and W are the length and width of the channel, C_i is the capacitance per unit area between the channel and bottom gate ($C_i = \varepsilon_0 \varepsilon_r / d_i$, ε_0: vacuum dielectric constant, ε_r: relative dielectric constant of SiO_2, d_i: the thickness of the dielectric layer), and dI_{ds}/dV_{gs} is the transconductance of transfer characteristic curves. The average hole mobility from 2D $In_2Ge_2Te_6$ FET devices (W = 5 μm and L = 6 μm) is ~43 cm^2 V^{-1} s^{-1}. The highest reported mobility of 2D $In_2Ge_2Te_6$ is approximately 43 cm^2 V^{-1} s^{-1}, which exceeds the mobility values of materials such as $CuAlO_2$, GaSe, and GeTe and is comparable to those of traditional and extensively studied p-type 2D semiconductors like WSe_2, TeO_2, and SnS (Table S3). Additionally, $In_2Ge_2Te_6$ exhibits a lower effective mass of 0.27 compared to the aforementioned materials. This suggests that 2D $In_2Ge_2Te_6$ has the potential for further enhancement in hole mobility. Although BP outperforms $In_2Ge_2Te_6$ in terms of mobility and effective mass, the superior air stability of $In_2Ge_2Te_6$ endows it with broader prospects for research and potential applications.[16−21] We also investigated the FET performance with different thicknesses of 2D $In_2Ge_2Te_6$ to illustrate the thickness-dependent evolution of hole mobility and on/off current ratio (Figures 4d and S16). The results indicate that the mobility of 2D $In_2Ge_2Te_6$ FET increased and then decreased with increasing thickness. The hole mobility reached its maximum at 13 nm and subsequently declined slightly with additional increases in thickness. Thinner samples are more susceptible to charge impurities at the interface and micro-nanofabrication processes, leading to lower hole mobility and on/off current ratio. The increased phonon density with thickness enhances carrier-phonon scattering, reducing carrier mean free path and consequently lowering mobility and on/off current ratio.[23] To investigate the electrical transport mechanism of 2D $In_2Ge_2Te_6$, we conducted temperature-dependent electrical measurements of the FET at 20−300 K (Figure 4e). Additionally, we plotted the calculated conductivity σ versus $1000/T$ curve, exhibiting a typical Arrhenius feature (Figure 4f). The data are fitted well using the double activation energies equation given by

$$\sigma = \sigma_1 \exp\left[-\frac{E_1}{k_B T}\right] + \sigma_2 \exp\left[-\frac{E_2}{k_B T}\right] \quad (4)$$

where σ_1 and σ_2 are conductance prefactors, E_1 and E_2 are two different activation energies in thermal activation and conduction, k_B is the Boltzmann constant, and T is temperature. The fitting results showed that E_1 and E_2 were 199.4 and 40.5 meV, respectively, corresponding to the deep and shallow acceptor states.[29,30] The temperature-dependent carrier transport reveals three distinct regimes with fundamentally different conduction mechanisms. We have identified distinct behaviors that are intricately linked to the activation of carriers across different temperature regimes. Specifically, we find that thermally activated carriers (holes) do not originate from shallow acceptor states but rather from deep acceptor states, which become increasingly active and dominate the conduction process above 200 K. In this high-temperature regime, intrinsic excitation is predominant, facilitating the migration of acceptor carriers to the VB through thermal activation, thereby enhancing the hole carrier concentration. In the intermediate temperature range of 100−200 K, carrier transport is governed by trap-assisted tunneling or variable-range hopping, indicative of significant trap states that impede carrier mobility. At lower temperatures (<100 K), impurity excitation emerges as the dominant mechanism, with minimal temperature dependence on conductivity.[31,32]

For this work, we have developed high-performance p-type FETs that utilize 2D $In_2Ge_2Te_6$ as the channel material. Our research shows that bulk $In_2Ge_2Te_6$ single crystals are intrinsic p-type semiconductors with a direct bandgap of 0.81 eV and an effective mass of 0.27. The 2D layered $In_2Ge_2Te_6$ nanosheets, obtained through exfoliation from the bulk material, demonstrate good air stability. The intrinsic p-type conduction arises from the differing binding forces of Ge−Ge for electrons in the z and xy directions. Our FET devices demonstrate thickness-dependent performance evolution, with field-effect hole mobility and on/off current ratio up to 43 cm^2 V^{-1} s^{-1} and 10^5 at room temperature (13 nm thick). We anticipate further improvements in FET device performance by reducing interface defects and lowering the Schottky barrier height. The discovery of 2D $In_2Ge_2Te_6$ provides a competitive p-type semiconductor for the 2D material family. It can potentially lead to the development of high-speed and low-power complementary logic circuits and vdW heterostructure devices.

■ ASSOCIATED CONTENT

Data Availability Statement

All relevant data supporting the findings of this study are available within the article and its Supporting Information and from the corresponding authors upon reasonable request.

Supporting Information

The Supporting Information is available free of charge at https://pubs.acs.org/doi/10.1021/acs.nanolett.5c00580.

Crystal synthesis, device manufacturing details, the XPS, PL, and tr ARPES characterization, material and device stability, hysteresis behavior and gate leakage currents (PDF)

■ AUTHOR INFORMATION

Corresponding Authors

Shengli Zhang − *MIIT Key Laboratory of Advanced Display Materials and Devices, Jiangsu Engineering Research Center for Quantum Dot Display, Institute of Optoelectronics & Nanomaterials, School of Materials Science and Engineering, Nanjing University of Science and Technology, Nanjing 210094, China;* orcid.org/0000-0003-4981-231X; Email: zhangslvip@njust.edu.cn

Xiang Chen − *MIIT Key Laboratory of Advanced Display Materials and Devices, Jiangsu Engineering Research Center for Quantum Dot Display, Institute of Optoelectronics & Nanomaterials, School of Materials Science and Engineering, Nanjing University of Science and Technology, Nanjing 210094, China;* orcid.org/0000-0001-5100-1482; Email: xiangchen@njust.edu.cn

Haibo Zeng − *MIIT Key Laboratory of Advanced Display Materials and Devices, Jiangsu Engineering Research Center for Quantum Dot Display, Institute of Optoelectronics & Nanomaterials, School of Materials Science and Engineering,*

https://doi.org/10.1021/acs.nanolett.5c00580
Nano Lett. 2025, 25, 6235−6243

Nanjing University of Science and Technology, Nanjing 210094, China; orcid.org/0000-0002-0281-3617; Email: zeng.haibo@njust.edu.cn

Authors

Tong Zhao − *MIIT Key Laboratory of Advanced Display Materials and Devices, Jiangsu Engineering Research Center for Quantum Dot Display, Institute of Optoelectronics & Nanomaterials, School of Materials Science and Engineering, Nanjing University of Science and Technology, Nanjing 210094, China*

Shiying Guo − *MIIT Key Laboratory of Advanced Display Materials and Devices, Jiangsu Engineering Research Center for Quantum Dot Display, Institute of Optoelectronics & Nanomaterials, School of Materials Science and Engineering, Nanjing University of Science and Technology, Nanjing 210094, China;* orcid.org/0000-0002-7772-7190

Xiufeng Song − *MIIT Key Laboratory of Advanced Display Materials and Devices, Jiangsu Engineering Research Center for Quantum Dot Display, Institute of Optoelectronics & Nanomaterials, School of Materials Science and Engineering, Nanjing University of Science and Technology, Nanjing 210094, China*

Jie Gao − *MIIT Key Laboratory of Advanced Display Materials and Devices, Jiangsu Engineering Research Center for Quantum Dot Display, Institute of Optoelectronics & Nanomaterials, School of Materials Science and Engineering, Nanjing University of Science and Technology, Nanjing 210094, China*

Kaili Wang − *National Laboratory of Solid State Microstructures, Collaborative Innovation Center of Advanced Microstructures, Nanjing University, Nanjing 210093, China*

Xudong Pei − *National Laboratory of Solid State Microstructures, Collaborative Innovation Center of Advanced Microstructures, Nanjing University, Nanjing 210093, China*

Yujie Yan − *National Laboratory of Solid State Microstructures, Collaborative Innovation Center of Advanced Microstructures, Nanjing University, Nanjing 210093, China*

Seungwoo Son − *Department of Materials Science and Engineering & Graduate School of Semiconductor Materials and Devices Engineering, Ulsan National Institute of Science and Technology (UNIST), Ulsan 44919, Republic of Korea; Center for Multidimensional Carbon Materials (CMCM), Institute for Basic Science (IBS), Ulsan 44919, Republic of Korea;* orcid.org/0000-0001-6003-4382

Jiamin Lin − *Key Laboratory of Mesoscopic Chemistry, School of Chemistry and Chemical Engineering, Nanjing University, Nanjing 210023, China*

Haonan Nie − *School of Chemistry and Chemical Engineering, Nanjing University of Science & Technology, Nanjing 210094, China*

Biao Xu − *School of Chemistry and Chemical Engineering, Nanjing University of Science & Technology, Nanjing 210094, China;* orcid.org/0000-0002-6645-3905

Zhesheng Chen − *MIIT Key Laboratory of Advanced Display Materials and Devices, Jiangsu Engineering Research Center for Quantum Dot Display, Institute of Optoelectronics & Nanomaterials, School of Materials Science and Engineering, Nanjing University of Science and Technology, Nanjing 210094, China*

Luca Perfetti − *Laboratoire des Solides Irradiés, CEA/DRF/IRAMIS, Ecole Polytechnique, CNRS, Institut Polytechnique de Paris, F-91128 Palaiseau, France;* orcid.org/0000-0002-8426-557X

Weigao Xu − *Key Laboratory of Mesoscopic Chemistry, School of Chemistry and Chemical Engineering, Nanjing University, Nanjing 210023, China;* orcid.org/0000-0002-3014-756X

Yi Zhang − *National Laboratory of Solid State Microstructures, Collaborative Innovation Center of Advanced Microstructures, Nanjing University, Nanjing 210093, China;* orcid.org/0000-0003-1204-8717

Zonghoon Lee − *Department of Materials Science and Engineering & Graduate School of Semiconductor Materials and Devices Engineering, Ulsan National Institute of Science and Technology (UNIST), Ulsan 44919, Republic of Korea; Center for Multidimensional Carbon Materials (CMCM), Institute for Basic Science (IBS), Ulsan 44919, Republic of Korea;* orcid.org/0000-0003-3246-4072

Peng Wang − *National Laboratory of Solid State Microstructures, Collaborative Innovation Center of Advanced Microstructures, Nanjing University, Nanjing 210093, China; Department of Physics, University of Warwick, CV4 7AL Coventry, U.K.*

Complete contact information is available at: https://pubs.acs.org/10.1021/acs.nanolett.5c00580

Author Contributions

T.Z., S.Y.G., and X.F.S. equally contributed to the design and execution of the experiments. T.Z. and J.G. were responsible for sample synthesis and characterization. T.Z. and X.F.S. designed and fabricated the FET devices. S.Y.G. and S.L.Z. performed DFT calculation. S.W.S., Z.H.L., X.D.P., Y.J.Y., and P.W. contributed to the HAADF-STEM test. Z.S.C., L.P., K.L.W., and Y.Z. performed ARPES measurement. J.M.L. and W.G.X. performed the Raman test. H.N.N. and B.X. contributed to the Seebeck coefficient measurement. T.Z. and X.C. wrote the manuscript. S.L.Z., X.C., and H.B.Z. supervised the project and contributed to discussions of the results. All authors discussed the results and provided feedback on the manuscript.

Notes

The authors declare no competing financial interest.

■ ACKNOWLEDGMENTS

This work was financially supported by the National Key Research and Development Program of China (2024YFB-3612400), National Natural Science Foundation of China (52372152, 92064007, 62274089, 52473236, U24A20286, 52131304, 62261160392), and Natural Science Foundation of Jiangsu Province (BZ2024038, BK20190476).

■ REFERENCES

(1) Wieting, T. J.; Verble, J. L. Interlayer bonding and the lattice vibrations of β-gase. *Phys. Rev. B* **1972**, *5* (4), 1473−1479.

(2) Frank, D. J.; Dennard, R. H.; Nowak, E.; Solomon, P. M.; Taur, Y.; Wong, H. S. P. Device scaling limits of Si Mosfets and their application dependencies. *P. IEEE* **2001**, *89* (3), 259−288.

(3) Theis, T. N.; Wong, H. S. P. The end of moore's law: A new beginning for information technology. *Comput. Sci. Eng.* **2017**, *19* (2), 41−50.

(4) Yoon, Y.; Ganapathi, K.; Salahuddin, S. How good can monolayer MoS_2 transistors be? *Nano Lett.* **2011**, *11* (9), 3768−73.

(5) Liu, L.; Lu, Y.; Guo, J. On monolayer MoS_2 field-effect transistors at the scaling limit. *IEEE Trans. Electron Devices* **2013**, *60* (12), 4133−4139.
(6) Liu, Y.; Weiss, N. O.; Duan, X.; Cheng, H.-C.; Huang, Y.; Duan, X. Van der waals heterostructures and devices. *Nat. Rev. Mater.* **2016**, *1* (9), 16042.
(7) Zhou, X.; Hu, X.; Zhou, S.; Zhang, Q.; Li, H.; Zhai, T. Ultrathin 2D $GeSe_2$ rhombic flakes with high anisotropy realized by van der waals epitaxy. *Adv. Funct. Mater.* **2017**, *27* (47), No. 1703858.
(8) Su, J.; Wang, M.; Li, Y.; Wang, F.; Chen, Q.; Luo, P.; Han, J.; Wang, S.; Li, H.; Zhai, T. Sub-millimeter-scale monolayer p-Type H-Phase VS_2. *Adv. Funct. Mater.* **2020**, *30* (17), No. 2000240.
(9) Choi, M. S.; Lee, M.; Ngo, T. D.; Hone, J.; Yoo, W. J. Chemical dopant-free doping by annealing and electron beam irradiation on 2D materials. *Adv. Funct. Mater.* **2021**, *7* (10), No. 2100449.
(10) Miao, N.; Li, W.; Zhu, L.; Xu, B.; Zhou, J.; Elliott, S. R.; Sun, Z. Tunable phase transitions and high photovoltaic performance of two-dimensional $In_2Ge_2Te_6$ semiconductors. *Nanoscale Horiz.* **2020**, *5* (12), 1566−1573.
(11) Lefèvre, R.; Berthebaud, D.; Lebedev, O.; Pérez, O.; Castro, C.; Gascoin, S.; Chateigner, D.; Gascoin, F. Layered tellurides: Stacking faults induce low thermal conductivity in the new $In_2Ge_2Te_6$ and thermoelectric properties of related compounds. *J. Mater. Chem. A* **2017**, *5* (36), 19406−19415.
(12) Chen, J.; Chen, H. Y.; Deng, W. T.; Gao, X.; Yin, S. Y.; Mei, Y.; Zhang, S.; Ni, L. S.; Gao, J. Q.; Liu, H. Q.; Tian, Y.; Yang, L.; Deng, X. L.; Zou, G. Q.; Hou, H. S.; Xie, J. Y.; Ji, X. B. Π-type orbital hybridization and reactive oxygen quenching induced by Se-doping for Li-rich Mn-based oxide cathode. *Energy Stor. Mater.* **2022**, *51*, 671−682.
(13) Shi, Y.; Ma, Z. R.; Xiao, Y. Y.; Yin, Y. C.; Huang, W. M.; Huang, Z. C.; Zheng, Y. Z.; Mu, F. Y.; Huang, R.; Shi, G. Y.; Sun, Y. Y.; Xia, X. H.; Chen, W. Electronic metal-support interaction modulates single-atom platinum catalysis for hydrogen evolution reaction. *Nat. Commun.* **2021**, *12* (1), DOI: 10.1038/s41467-021-23306-6.
(14) Fang, H.; Chuang, S.; Chang, T. C.; Takei, K.; Takahashi, T.; Javey, A. High-performance single layered WSe_2 p-FETs with chemically doped contacts. *Nano Lett.* **2012**, *12* (7), 3788−3792.
(15) Chen, W.; Hu, M.; Zong, J.; Xie, X.; Meng, Q.; Yu, F.; Wang, L.; Ren, W.; Chen, A.; Liu, G.; Xi, X.; Li, F.-S.; Sun, J.; Liu, J.; Zhang, Y. Epitaxial growth of single-phase 1T′-WSe_2 monolayer with assistance of enhanced interface interaction. *Adv. Mater.* **2021**, *33* (7), No. 2004930.
(16) Sucharitakul, S.; Kumar, U. R.; Sankar, R.; Chou, F.-C.; Chen, Y.-T.; Wang, C.; He, C.; He, R.; Gao, X. P. A. Screening limited switching performance of multilayer 2D semiconductor FETs: the case for SnS. *Nanoscale* **2016**, *8* (45), 19050−19057.
(17) Suzuki, I.; Lin, Z.; Kawanishi, S.; Tanaka, K.; Nose, Y.; Omata, T.; Tanaka, S.-I. Direct evaluation of hole effective mass of SnS-SnSe solid solutions with arpes measurement. *Phys. Chem. Chem. Phys.* **2022**, *24* (2), 634−638.
(18) Zalamai, V. V.; Rusu, E. V.; Syrbu, N. N.; Tiron, A. V. Optical properties and electronic band structure of SnS single crystals. *Physica B Condens.* **2019**, *575*, No. 411712.
(19) Kim, Y.-M.; Hong, S.; Yoon, Y.; Kim, S.; Cho, H.; Sritharan, M.; Ju, Y.; Pujar, P.; Dutta, R.; Jang, W.-S. Se-Vacancy Healing with Substitutional Oxygen in WSe_2 for High-Mobility p-Type Field-Effect Transistors. *ACS Nano* **2023**, *17* (12), 11279−11289.
(20) Feng, X.; Huang, X.; Chen, L.; Tan, W. C.; Wang, L.; Ang, K.-W. High Mobility Anisotropic Black Phosphorus Nanoribbon Field-Effect Transistor. *Adv. Funct. Mater.* **2018**, *28* (28), No. 1801524.
(21) Margot, F.; Lisi, S.; Cucchi, I.; Cappelli, E.; Hunter, A.; Gutierrez-Lezama, I.; Ma, K.; von Rohr, F.; Berthod, C.; Petocchi, F.; Ponce, S.; Marzari, N.; Gibertini, M.; Tamai, A.; Morpurgo, A. F.; Baumberger, F. Electronic Structure of Few-Layer Black Phosphorus from μ-ARPES. *Nano Lett.* **2023**, *23* (14), 6433−6439.
(22) Li, J.; Zhang, Y.; Zhang, J.; Chu, J.; Xie, L.; Yu, W.; Zhao, X.; Chen, C.; Dong, Z.; Huang, L.; Yang, L.; Yu, Q.; Ren, Z.; Wang, J.; Xu, Y.; Zhang, K. Chemical Vapor Deposition of Quaternary 2D BiCuSeO p-Type Semiconductor with Intrinsic Degeneracy. *Adv. Mater.* **2022**, *34* (50), No. 2207796.
(23) Lu, W. L.; Nan, H. Y.; Hong, J. H.; Chen, Y. M.; Zhu, C.; Liang, Z.; Ma, X. Y.; Ni, Z. H.; Jin, C. H.; Zhang, Z. Plasma-assisted fabrication of monolayer phosphorene and its Raman characterization. *Nano Res.* **2014**, *7* (6), 853−859.
(24) Mahlouji, R.; Verheijen, M. A.; Zhang, Y.; Hofmann, J. P.; Kessels, W. M. M.; Bol, A. A. Thickness and Morphology Dependent Electrical Properties of ALD-Synthesized MoS_2 FETs. *Adv. Electron. Mater.* **2022**, *8* (3), No. 2100781.
(25) Sun, X.; Yu, B.; Ng, G.; Meyyappan, M. One-dimensional phase-change nanostructure: Germanium telluride nanowire. *J. Phys. Chem. C* **2007**, *111* (6), 2421−2425.
(26) Zhang, P.; Zhao, F.; Long, P.; Wang, Y.; Yue, Y.; Liu, X.; Feng, Y.; Li, R.; Hu, W.; Li, Y.; Feng, W. Sonication-assisted liquid-phase exfoliated alpha-GeTe: a two-dimensional material with high Fe^{3+} sensitivity. *Nanoscale* **2018**, *10* (34), 15989−15997.
(27) Chaves, A.; Azadani, J. G.; Alsalman, H.; da Costa, D. R.; Frisenda, R.; Chaves, A. J.; Song, S. H.; Kim, Y. D.; He, D.; Zhou, J.; Castellanos-Gomez, A.; Peeters, F. M.; Liu, Z.; Hinkle, C. L.; Oh, S.-H.; Ye, P. D.; Koester, S. J.; Lee, Y. H.; Avouris, P.; Wang, X.; Low, T. Bandgap engineering of two-dimensional semiconductor materials. *NPJ. 2D Mater. Appl.* **2020**, *4* (1), DOI: 10.1038/s41699-020-00162-4.
(28) Wang, Z.; Nayak, P. K.; Caraveo-Frescas, J. A.; Alshareef, H. N. Recent Developments in p-Type Oxide Semiconductor Materials and Devices. *Adv. Mater.* **2016**, *28* (20), 3831−3892.
(29) Wu, F.; Gutierrez-Lezama, I.; Lopez-Paz, S. A.; Gibertini, M.; Watanabe, K.; Taniguchi, T.; von Rohr, F. O.; Ubrig, N.; Morpurgo, A. F. Quasi-1D Electronic Transport in a 2D Magnetic Semiconductor. *Adv. Mater.* **2022**, *34* (16), No. 2109759.
(30) Xu, J.; Chang, Y.; Gan, L.; Ma, Y.; Zhai, T. ltrathin Single-Crystalline Boron Nanosheets for Enhanced Electro-Optical Performances. *Adv. Sci.* **2015**, *2* (6), No. 1500023.
(31) Zheng, Z.; Gan, L.; Li, H.; Ma, Y.; Bando, Y.; Golberg, D.; Zhai, T. Fully Transparent and Flexible Ultraviolet−Visible Photodetector Based on Controlled Electrospun ZnO-CdO Heterojunction Nanofi ber Arrays. *Adv. Funct. Mater.* **2015**, *25* (37), 5885−5894.
(32) Yang, S.; Liu, K.; Han, W.; Li, L.; Wang, F.; Zhou, X.; Li, H.; Zhai, T. Salt-Assisted Growth of P-type Cu9S5 Nanoflakes for P-N Heterojunction Photodetectors with High Responsivity. *Adv. Funct. Mater.* **2020**, *30* (7), No. 1908382.

https://doi.org/10.1021/acs.nanolett.5c00580
Nano Lett. 2025, 25, 6235−6243